

Revealing the Dominant Source of Cosmic Rays in a Nearby Galaxy

Tomonari Michiyama (✉ t.michiyama.astr@gmail.com)

Osaka University <https://orcid.org/0000-0003-2475-7983>

Yoshiyuki Inoue

Osaka University <https://orcid.org/0000-0002-7272-1136>

Akihiro Doi

Institute of Space and Astronautical Science, Japan Aerospace Exploration Agency

Dmitry Khangulyan

Rikkyo University <https://orcid.org/0000-0002-7576-7869>

Article

Keywords:

Posted Date: March 28th, 2022

DOI: <https://doi.org/10.21203/rs.3.rs-1437140/v1>

License: © ⓘ This work is licensed under a Creative Commons Attribution 4.0 International License.

[Read Full License](#)

1 Revealing the Dominant Source of Cosmic Rays in a Nearby Galaxy

2 We request double blind peer review¹,

3 ¹TBD

4 **Cosmic rays are ultrarelativistic particles that are integral components of the cosmic background. The cosmic-**
5 **ray energy spectrum suggests the existence of so-called galactic PeVatrons— local sources that are capable of**
6 **boosting the particle energy beyond 1 PeV^{1,2}. In the Milky Way, the birth and death of massive stars give rise**
7 **to sufficient cosmic-ray sources for supplying the required accelerating power. Through observations in the**
8 **gamma-ray band, several nearby galaxies with cosmic ray power significantly exceeding the calorimetric limit**
9 **of the star formation activities have been identified^{3–6} such as NGC 1068, which is a nearby Seyfert galaxy^{7–9}.**
10 **Compared to other galaxies, NGC 1068 features a modest-power kiloparsec-scale jet and one of the most active**
11 **regions surrounding the central supermassive black hole^{10,11}. While synchrotron emission was confirmed at**
12 **the jet by centimetre interferometers, the particle spectrum and acceleration site could not be identified due to**
13 **limited frequency coverage and angular resolution. Here we report the high-resolution radio observations of**
14 **NGC 1068, which reveal the ultrarelativistic electrons at the apex of its jet. Spectral and morphological studies**
15 **of the parsec-scale radio blobs in the jet termination region show that these blobs are efficient sites of cosmic-ray**
16 **acceleration with a strongly amplified magnetic field. The physical conditions revealed in the blobs imply that**
17 **they are capable of accelerating protons to energies beyond the petaelectronvolt range. The estimated cosmic-**
18 **ray power at the jet head exceeds the limit set by the star formation activity in this galaxy. This result suggests**
19 **that even modest-power jets significantly increase the galactic cosmic-ray content while propagating through**
20 **the galactic bulge.**

21 The direct observation of cosmic rays is performed over a broad range of energies from 10⁹ eV to 10²¹ eV and
22 even beyond^{1,2}. The measured spectrum indicates the existence of a component that contains the bulk of the cosmic-
23 ray energy and extends to the “knee,” which is a spectral break found at petaelectronvolt-scale energies. Thus, it is
24 necessary to understand the galactic cosmic accelerators operating in this energy range. Unveiling the cosmic-ray
25 production activities in galaxies is also important for studying the galaxy evolution, as shown in recent cosmological
26 simulations^{12,13}. Diffusive shock acceleration (DSA) is the most feasible acceleration mechanism in various astro-
27 physical environments and systems^{14,15}. For example, supernovae explosions, which drive quasi-spherical blast waves
28 propagating through the interstellar medium (ISM) with a typical speed of several thousand kilometers per second, are
29 known as efficient DSA sites and are considered the best PeVatron candidates in the Milky Way^{16,17}.

30 Because cosmic rays produce electromagnetic emissions through interactions with the surrounding gas, photons,
31 and magnetic fields, we can observe cosmic-ray factories in other galaxies as well. The cosmic-ray level in some of
32 the observed galaxies is consistent with that of the Milky Way. For example, the detected gamma-ray flux in nearby
33 starburst galaxies, such as NGC 253 and M 82, is reasonably explained by supernova activity^{3–5}. However, several
34 nearby galaxies exhibit an excess gamma-ray flux above the calorimetric limit of their star formation activity^{6,8}.

35 NGC 1068, located at a distance of $D_L = 16$ Mpc from the sun (1 arcsec ≈ 77 pc), is one of the brightest gamma-
36 ray emitters among nonblazar galaxies¹⁸, and its starburst activity falls below the detected gamma-ray flux level^{7,8}.
37 In addition, hints of the high-energy neutrino from the direction of NGC 1068 are recently reported¹⁹. Therefore,
38 this galaxy is an ideal target for investigating alternative cosmic-ray sources, other than those driven by the star
39 formation activity. NGC 1068 is a Seyfert galaxy with an active galactic nucleus (AGN), i.e. the vicinity of its
40 central supermassive black hole (SMBH) is active^{20,21}. In addition, this galaxy has a prominent linear radio structure
41 with an extent of 13 arcsec^{10,11}, and is associated with a jet with a power of $P_{\text{jet}} = 1.8 \times 10^{43}$ erg s⁻¹, known as
42 kiloparsec-scale jet^{21,22}. Self-similar fluid models developed for extragalactic jet sources²³ allow estimating the jet
43 age and expanding velocity as $t_{\text{jet}} \approx 1.3 \times 10^5$ yr and $v_{\text{exp}} \approx 3.0 \times 10^3$ km s⁻¹, respectively (see Methods for the
44 detail). Previous observations by centimetre interferometers, e.g. those with Very Large Array (VLA), show bright
45 synchrotron emission from high-energy electrons at the jet¹⁰. However, owing to the limited frequency coverage and

46 angular resolution, the particle spectrum and acceleration site could not be identified.

47 Here, we analysed the archival centimetre and millimetre data of NGC 1068 using VLA and the Atacama Large
 48 Millimeter/submillimeter Array (ALMA). Figure 1 shows the low (~ 0.4 arcsec, 30 pc) and high (~ 0.05 arcsec,
 49 4 pc) resolution millimetre maps of NGC 1068 obtained by ALMA. The low-resolution map obtained at 93.5 GHz
 50 (Figure 1a) displays a kiloparsec-scale radio lobe (hereafter NE-Lobe), indicating the shock formed by the interaction
 51 of the jet with the ISM at the edge of NE-Lobe. The brightest radio emission comes from the head of the NE-Lobe.
 52 Figure 1b and 1c display the high-resolution 92 GHz map of the entire NE-Lobe region and the enlarged view of
 53 the head of the NE-Lobe, respectively. This ALMA high-resolution map shows the bright region at the head of the
 54 NE-Lobe resolved into several blobs. Using the archival 15 GHz VLA and 252 GHz ALMA maps with an angular
 55 resolution of ≈ 0.15 arcsec, we measured the local spectral index, $\alpha \equiv -dS_\nu/d\nu$ and obtained values ranging
 56 between $\alpha = 0.47$ and 0.65 from the resolved blobs (see the Methods for details). The spatial intensity profile from
 57 the central black hole to the peak position at the head is presented in Figure 2. The blob diameter is defined as the full
 58 width at half maximum (FWHM) of the spatial profile. For the brightest blob, we obtained $d_b \approx 12$ pc, which exceeds
 59 the beam size by a factor of three. The 92 GHz flux density associated with the brightest blob is ≈ 0.77 mJy (0.15
 60 arcsec aperture in diameter) corresponding to a specific luminosity of $L_{92\text{GHz}} \approx 2.5 \times 10^{19}$ W Hz $^{-1}$.

Unless the plasma density is unfeasibly high, $n > 10^3$ cm $^{-3}$, the detected radio emission is a synchrotron origin
 that is produced by relativistic electrons interacting with a magnetic field. Assuming a power-law electron energy
 distribution, $n(E)dE \propto E^{-p}dE$, the electron power-law index of $p \approx 2$ (note that $p = 2\alpha + 1$) can be determined
 from the obtained radio spectra. For the total energy of the magnetic field and radio-emitting electrons to be close to the
 minimum value, which approximately corresponds to the energy equipartition between the magnetic field and radio-
 emitting electrons (see the Methods section for details), we can estimate the magnetic field strength in the brightest
 blob²⁴:

$$B_{\text{eq}} \approx 230 \mu\text{G} \left(\frac{L_{92\text{GHz}}}{2.5 \times 10^{19} \text{ W Hz}^{-1}} \right)^{\frac{2}{7}} \left(\frac{V}{8.7 \times 10^2 \text{ pc}^3} \right)^{-\frac{2}{7}}. \quad (1)$$

61 Here, we assumed a spherical volume with a diameter of 12 pc. This magnetic field strength is significantly higher
 62 than that of the ISM (a few μG)²⁵, suggesting a strongly amplified magnetic field. Such a magnetic field amplification
 63 is observed in Galactic supernova remnants, where cosmic-ray streaming enhances the ISM magnetic field up to a few
 64 hundred μG (see Eq. 29 in Ref.²⁶).

Locally accelerated electrons lose their energy owing to synchrotron cooling over a time scale of

$$t_{\text{sync}} = \frac{3}{4} \frac{m_e c}{\sigma_T U_B} \gamma_e^{-1} \approx 2.8 \times 10^4 \text{ yr} \left(\frac{B}{230 \mu\text{G}} \right)^{-\frac{3}{2}} \left(\frac{\nu_{\text{sync}}}{92 \text{ GHz}} \right)^{-\frac{1}{2}}. \quad (2)$$

65 Here, $\nu_{\text{sync}} = 3eB\gamma_e^2/4\pi m_e c$, where m_e is the electron rest mass, σ_T is the Thomson scattering cross-section, and e
 66 is the elementary charge. For comparison, the advection timescale through the blob is $t_{\text{adv}} = d_b/v_d \approx 1.6 \times 10^4$ yr
 67 (adopting downstream speed, $v_d = v_{\text{exp}}/4$, expected for strong shocks). Given that $t_{\text{adv}} \lesssim t_{\text{sync}}$, synchrotron emission
 68 is produced in the slow-cooling regime; that is, we observe the emission of freshly accelerated electrons. The measured
 69 electron spectrum, $p \approx 2$, is consistent with the canonical slope predicted for DSA under a strong shock^{14,15}.

70 The bright synchrotron emission of non-thermal electrons at the shock also implies efficient acceleration of the
 71 protons. The required amplification of the magnetic field is possible, for example, by nonresonant hybrid instability²⁶,
 72 if a significant current is generated at upstream by the cosmic-ray particles. This implies that a considerable fraction
 73 of the downstream energy is transferred to relativistic protons. Because the physical conditions revealed at the forward
 74 shock are similar to those at the blast wave produced by a supernovae explosion, we can readily use the estimates
 75 for the cosmic-ray maximum energy from the literature. Adopting Eq. 6 from Ref.²⁶, the parameters of the shock in
 76 NGC 1068 (most critically, the age and shock speed) suggest $E_{\text{cr,max}} \approx 8$ PeV (see Methods for details).

77 The VLA and ALMA data allow us to obtain the total electron power as $P_e \approx \pi(d_b/2)^2 v_d U_e \approx 2.1 \times 10^{38} \text{ erg s}^{-1}$
78 per a radio-emitting blob. Here, we use the equipartition condition to derive electron energy density U_e . This estimate
79 for P_e implies that the total cosmic-ray accelerating power in NGC 1068 can be as large as $P_{\text{CR,blobs}} \approx 1.7 \times$
80 $10^{41} \text{ erg s}^{-1}$, where we summed the contributions from the four detected blobs, accounted for the existence of the
81 counter jet, and adopted the standard electron-to-proton energy ratio ($K_{\text{ep}} \approx 0.01$)²⁷. The expected power available for
82 the cosmic-ray acceleration is $\approx 1\%$ of the jet power, which is comparable to the efficiency of cosmic-ray acceleration
83 produced by supernovae remnants. Notably this value of $P_{\text{CR,blobs}}$ corresponds to the lower limit of the total cosmic-
84 ray accelerating power of this jet ($P_{\text{CR,jet}}$), because we neglect the cosmic-ray acceleration occurring outside the blobs
85 resolved by ALMA, i.e. $P_{\text{CR,jet}} > P_{\text{CR,blobs}}$.

86 The total cosmic-ray accelerating power of the supernovae in NGC 1068 can be estimated as $P_{\text{CR,SN}} \approx 2 \times$
87 $10^{41} \text{ erg s}^{-1}$ (the observed supernovae rate is 0.07 per year^{8,28}, the energy of a supernova is 10^{51} erg , and 10 % of
88 supernova energy is transferred to the cosmic rays). The relation of $P_{\text{CR,jet}} > P_{\text{CR,blobs}} \approx P_{\text{CR,SN}}$ indicates that the
89 resolved parsec-scale blobs in the termination region of the kiloparsec-scale jet can be dominant sources of cosmic-
90 ray production activities, other than the star formation activities in NGC 1068 and would contribute to the gamma-ray
91 excess seen in this galaxy. Considering the spectral shape, maximum energy, and total energy budget, the blobs at the
92 kiloparsec-scale jet head are presumed to be a cosmic-ray factory.

93 The high-spatial-resolution ALMA image of the kiloparsec-scale jet in NGC 1068 enabled us to reveal a new
94 dominant cosmic-ray factory. Approximately one-third of all Seyfert galaxies have similar elongated linear radio
95 structures²⁹, and many other galaxies experience active phases, such as these AGNs. Therefore, low-power AGN
96 jets could be the dominant sources of galactic cosmic rays. Future high-spatial-resolution ALMA observations of
97 kiloparsec-scale jets in other nearby Seyfert galaxies, such as IC 5063, NGC 5643, and NGC 1386³⁰ will reveal
98 details of the roles of the kiloparsec-scale jet in cosmic rays production and its impact on the evolution of galaxies.
99 For example, recent cosmological simulations have been investigating how the cosmic-ray injection impacts the bulk
100 properties of galaxies. However, only supernovae are accounted as the direct process of the cosmic-ray injections
101 within galaxies, suggesting weak effects on galaxy properties^{12,13}. Revealing the cosmic-rays production by kiloparsec-
102 scale jet can be a key to understand the direct effect of cosmic-ray feedback within the galaxies by AGNs (not by the
103 supernovae).

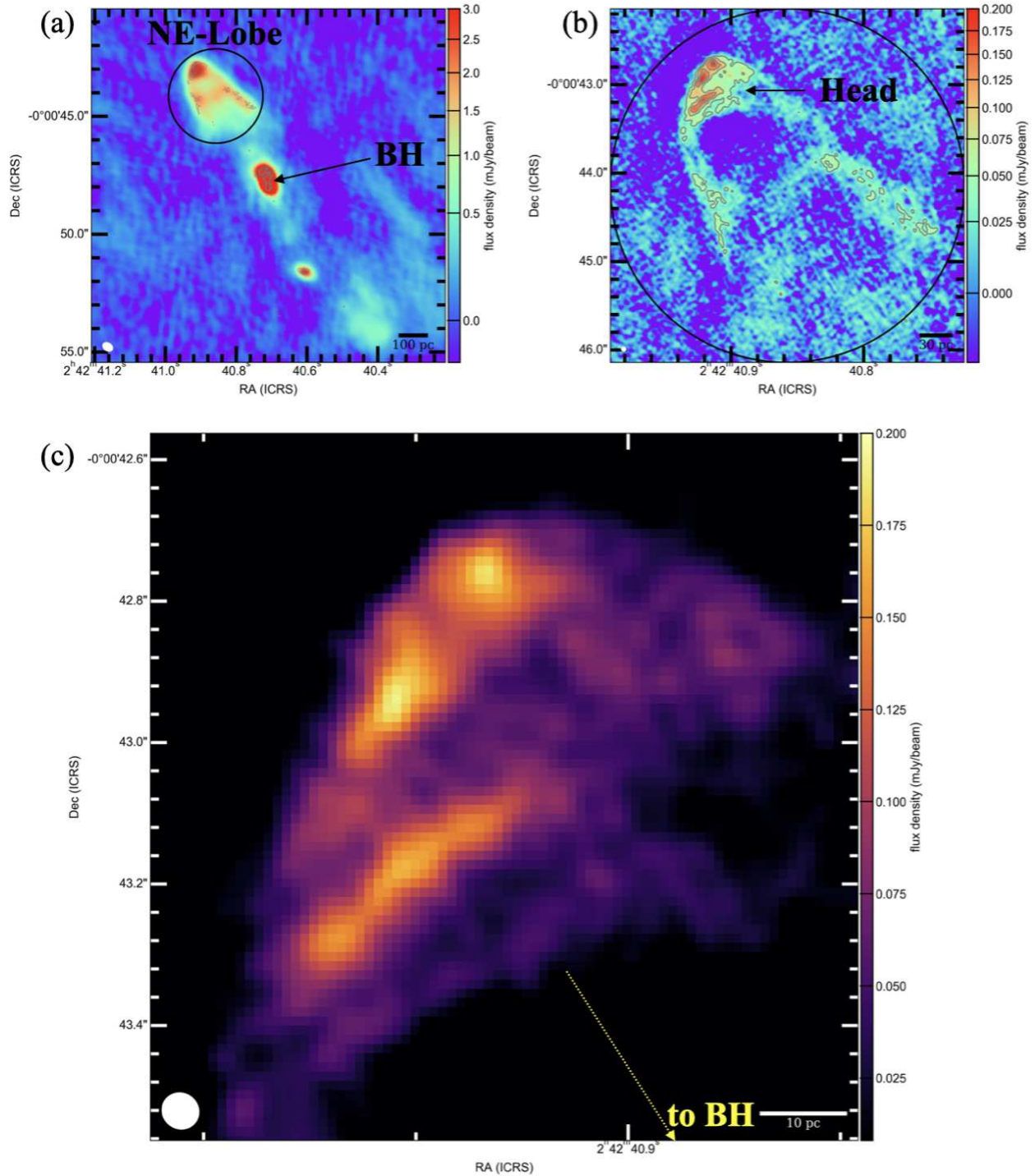


Figure 1: (a) ALMA low-resolution (synthesized beam is 0.46×0.34 arcsec²) 93 GHz map. The solid black circle indicates the 4 arcsec aperture. (b) ALMA high-resolution (synthesized beam is 0.053×0.050 arcsec²) 92 GHz map. To highlight the image noise, the colour was scaled by a square-root stretch. (c) Enlarged views around the head of the NE-Lobe. The dashed yellow arrow indicates the direction of the central SMBH. To highlight the two arcs, the colour was scaled linearly. For (a) and (b), the grey contour level is $(5, 10, 15, 20) \times \sigma$, where $\sigma = 8 \mu\text{Jy beam}^{-1}$ is the noise level of the high-resolution map. For (a)-(c), the white ellipse at the bottom left corner represents the synthesized beam, and the black and white bars at the bottom right corner represent the physical scale bar.

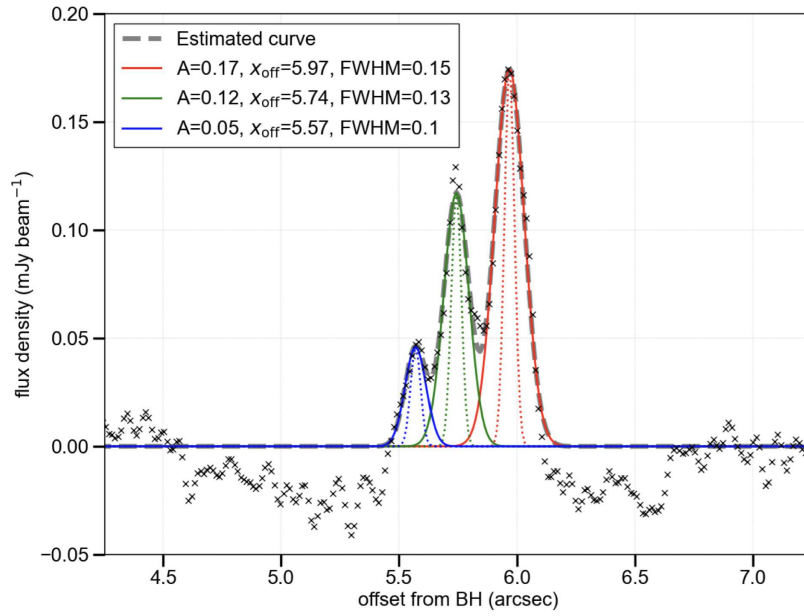


Figure 2: One-dimensional 92 GHz brightness profile along the extended yellow dashed arrow in Figure 1. The profile (black crosses) was fitted by three Gaussian distribution functions (red, green, and blue solid lines). A , x_{off} , and FWHM in the graph legends correspond to the amplitude (Jy beam^{-1}), peak position (arcsec), and emission width (arcsec) obtained from the FWHM of the best fit Gaussians peak, respectively. The grey dashed line indicates the summation of the three Gaussian profiles. The dotted red, green, and blue lines indicate the three sources with the FWHM of 0.05 arcsec (i.e., synthesized beam), suggesting that the structure along the jet direction is spatially resolved.

104

105

107

108

109

110

111

112

113

114

115

116

117

118

119

120

121

122

123

124

125

126

127

128

129

130

131

132

133

134

135

136

137

138

139

140

141

142

143

-
1. Blasi, P. The origin of galactic cosmic rays. *A&A Rev.* **21**, 70 (2013). 1311.7346.
 2. Kotera, K. & Olinto, A. V. The Astrophysics of Ultrahigh-Energy Cosmic Rays. *Annual Review of Astronomy and Astrophysics* **49**, 119–153 (2011). 1101.4256.
 3. Persic, M., Rephaeli, Y. & Arieli, Y. Very-high-energy emission from M 82. *Astron. Astrophys.* **486**, 143–149 (2008).
 4. Rephaeli, Y., Arieli, Y. & Persic, M. High-energy emission from the starburst galaxy NGC 253. *Mon. Not. R. Astron. Soc.* **401**, 473–478 (2010). 0906.1921.
 5. Abdo, A. A. *et al.* Search for Gamma-ray Emission from Magnetars with the Fermi Large Area Telescope. *Astrophys. J. Lett.* **725**, L73–L78 (2010). 1011.0091.
 6. Ajello, M., Di Mauro, M., Paliya, V. S. & Garrappa, S. The γ -Ray Emission of Star-forming Galaxies. *Astrophys. J.* **894**, 88 (2020). 2003.05493.
 7. Lenain, J. P., Ricci, C., Türler, M., Dorner, D. & Walter, R. Seyfert 2 galaxies in the GeV band: jets and starburst. *Astron. Astrophys.* **524**, A72 (2010). 1008.5164.
 8. Eichmann, B. & Becker Tjus, J. The Radio-Gamma Correlation in Starburst Galaxies. *Astrophys. J.* **821**, 87 (2016). 1510.03672.
 9. Acciari, V. A. *et al.* Constraints on Gamma-Ray and Neutrino Emission from NGC 1068 with the MAGIC Telescopes. *Astrophys. J.* **883**, 135 (2019). 1906.10954.
 10. Wilson, A. S. & Ulvestad, J. S. A Radiative Bow Shock Wave (?) Driven by Nuclear Ejecta in a Seyfert Galaxy. *Astrophys. J.* **319**, 105 (1987).
 11. Gallimore, J. F., Baum, S. A. & O’Dea, C. P. The Subarcsecond Radio Structure in NGC 1068. II. Implications for the Central Engine and Unifying Schemes. *Astrophys. J.* **464**, 198 (1996).
 12. Hopkins, P. F. *et al.* But what about...: cosmic rays, magnetic fields, conduction, and viscosity in galaxy formation. *Mon. Not. R. Astron. Soc.* **492**, 3465–3498 (2020). 1905.04321.
 13. Hopkins, P. F. *et al.* Testing physical models for cosmic ray transport coefficients on galactic scales: self-confinement and extrinsic turbulence at \sim GeV energies. *Mon. Not. R. Astron. Soc.* **501**, 4184–4213 (2021). 2002.06211.
 14. Blandford, R. D. & Ostriker, J. P. Particle acceleration by astrophysical shocks. *Astrophys. J. Lett.* **221**, L29–L32 (1978).
 15. Bell, A. R. The acceleration of cosmic rays in shock fronts - I. *Mon. Not. R. Astron. Soc.* **182**, 147–156 (1978).
 16. Uchiyama, Y., Aharonian, F. A., Tanaka, T., Takahashi, T. & Maeda, Y. Extremely fast acceleration of cosmic rays in a supernova remnant. *Nature* **449**, 576–578 (2007).
 17. Tsuji, N. *et al.* NuSTAR Observations of the Supernova Remnant RX J1713.7-3946. *Astrophys. J.* **877**, 96 (2019). 1904.12436.
 18. Ackermann, M. *et al.* GeV Observations of Star-forming Galaxies with the Fermi Large Area Telescope. *Astrophys. J.* **755**, 164 (2012). 1206.1346.
 19. Aartsen, M. G. *et al.* Time-Integrated Neutrino Source Searches with 10 Years of IceCube Data. *Phys. Rev. Lett.* **124**, 051103 (2020). 1910.08488.

- 144 20. Antonucci, R. R. J. & Miller, J. S. Spectropolarimetry and the nature of NGC 1068. *Astrophys. J.* **297**, 621–632
145 (1985).
- 146 21. García-Burillo, S. *et al.* Molecular line emission in NGC 1068 imaged with ALMA. I. An AGN-driven outflow
147 in the dense molecular gas. *Astron. Astrophys.* **567**, A125 (2014). 1405.7706.
- 148 22. Bîrzan, L., McNamara, B. R., Nulsen, P. E. J., Carilli, C. L. & Wise, M. W. Radiative Efficiency and Con-
149 tent of Extragalactic Radio Sources: Toward a Universal Scaling Relation between Jet Power and Radio Power.
150 *Astrophys. J.* **686**, 859–880 (2008). 0806.1929.
- 151 23. Kaiser, C. R. & Alexander, P. A self-similar model for extragalactic radio sources. *Mon. Not. R. Astron. Soc.* **286**,
152 215–222 (1997).
- 153 24. Longair, M. S. *High Energy Astrophysics* (2011).
- 154 25. Ferrière, K. M. The interstellar environment of our galaxy. *Reviews of Modern Physics* **73**, 1031–1066 (2001).
155 astro-ph/0106359.
- 156 26. Bell, A. R., Schure, K. M., Reville, B. & Giacinti, G. Cosmic-ray acceleration and escape from supernova
157 remnants. *Mon. Not. R. Astron. Soc.* **431**, 415–429 (2013). 1301.7264.
- 158 27. Hillas, A. M. TOPICAL REVIEW: Can diffusive shock acceleration in supernova remnants account for high-
159 energy galactic cosmic rays? *Journal of Physics G Nuclear Physics* **31**, R95–R131 (2005).
- 160 28. Storchi-Bergmann, T. *et al.* Two-dimensional Mapping of Young Stars in the Inner 180 pc of NGC 1068: Corre-
161 lation with Molecular Gas Ring and Stellar Kinematics. *Astrophys. J.* **755**, 87 (2012). 1206.4014.
- 162 29. Kellermann, K. I., Sramek, R., Schmidt, M., Shaffer, D. B. & Green, R. VLA Observations of Objects in the
163 Palomar Bright Quasar Survey. *AJ* **98**, 1195 (1989).
- 164 30. Venturi, G. *et al.* MAGNUM survey: Compact jets causing large turmoil in galaxies. Enhanced line widths
165 perpendicular to radio jets as tracers of jet-ISM interaction. *Astron. Astrophys.* **648**, A17 (2021). 2011.04677.

166 Methods

167 A Target

168 NGC 1068 is an archetypal Seyfert 2 galaxy located at $D_L = 16$ Mpc from the sun. We used the `Astropy`^{31,32}
169 sub-package to calculate commonly used quantities that depend on a cosmological model with parameters from the
170 nine-year Wilkinson Microwave Anisotropy Probe results. Under this assumption, 1 arcsec corresponds to 77 pc at
171 NGC 1068 ($z=0.0037$). The 20 cm (1.5 GHz) radio power is $\log P_{1.5\text{GHz}} = 23.37 \text{ W Hz}^{-1}$, which is one of the
172 brightest galaxies in the radio band among the nearby Seyfert galaxies^{33,34}. A linear radio source with an extent of
173 13 arcsec was confirmed (northeast and southwest lobe) by VLA, and is explained by the kiloparsec-scale collimated
174 ejection from the Seyfert nucleus, either quasi-continuously or as a “jet”^{35,36}. The structure along the radio jet axis
175 was investigated using a wide range of wavelengths from X-rays to radio waves^{37–40}. For example, [OIII] plumes were
176 detected in the northeast but not in the southwest. This implies that the northeast ionised cone illuminates the near
177 side of the disk, whereas the southwest cone illuminates the backside. This geometry can also explain the asymmetry
178 in the X-rays (e.g. ROSAT HRI)³⁸. The red- and blue-shifted high- and low-ionisation lines (optical lines) suggest
179 that the radio lobes encounter diffuse material located outside the galactic plane (traced by a high ionisation line)
180 and sweep denser molecular disks (traced by the low-ionisation line)^{39,40}. In addition, molecular gas outflows traced
181 by CO lines were also detected where the ionised cone sweeps the molecular disk³⁵. However, understanding the
182 complicated lobe–ISM interaction structure explained above is beyond the scope of this study. In this letter, we focus
183 on the parsec-scale 92 GHz continuum structure at the “head” of the radio lobe.

184 B Jet properties

185 We measured the distance from the central black hole to the tip of the NE-Lobe ($l_{\text{jet}} \approx 670$ pc), assuming that
186 the jet inclination against our line of sight is 45° . A jet power of $P_{\text{jet}} = 1.8 \times 10^{43} \text{ erg s}^{-1}$ was estimated from the
187 monochromatic luminosity at 1.4 GHz, reported in the literature^{35,41}. We assumed a self-similar fluid model developed
188 for extragalactic jet sources^{42,43}, where the jet supplies energy at a constant rate (P_{jet}) and expands with a velocity
189 of v_{exp} in a medium of constant mass density $\mu\bar{n}$ (μ is the average particle mass of $0.68m_{\text{H}}$, m_{H} is the hydrogen
190 mass, and \bar{n} is the average particle density). Subsequently, the jet age is given as $t_{\text{jet}} = (l_{\text{jet}}/2)^{5/3}(\mu\bar{n}/P_{\text{jet}})^{1/3}$ by
191 balancing the interior pressure and ram pressure of the shocked ISM. By differentiating both sides of the equation with
192 respect to time, the lobe expansion velocity can be obtained as $v_{\text{exp}} = (3/5)(l_{\text{jet}}/t_{\text{jet}})$; for NGC 1068, we obtained
193 $t_{\text{jet}} \approx 1.3 \times 10^5 \text{ yr}$ and $v_{\text{exp}} \approx 3.0 \times 10^3 \text{ km s}^{-1}$.

194 C Data

195 We used archival VLA and ALMA data to investigate the centimetre-to-millimetre properties of the compact jet. We
196 used the archival FITS image files (not visibility) obtained from the NRAO VLA Archive Survey and Japanese Virtual
197 Observatory (JVO). We selected low- and high-resolution images (Extended Data Figures 1 and 2 and Table 1) as well
198 as all processed images were primary beam corrected. We did not use ALMA higher frequency data (e.g. bands 7 and
199 8) because of the lack of archival data showing robust detection of NE-Lobe owing to sensitivity issues. In addition,
200 contamination from dust emissions, which are associated with molecular disks wherein CO outflows are detected³⁵,
201 increased at high frequencies. We confirmed that the jet head and molecular disk were spatially separated; thus, the
202 contamination of dust emissions in band 6 data was negligible. As shown in Extended Data Figures (1) and (2) in the
203 main text, negative values were observed in some pixels around the jet head. This is owing to the sidelobes, which
204 could not be removed using deconvolution processes (i.e. clean parameters during the QA2 process by the ALMA
205 observatory and our own manual masking for the clean task). The negative components may be removed using self-
206 calibration techniques; however, the parameters of the resulting images (e.g. clumpiness and peak flux density) are
207 affected. Because the image quality itself did not affect the main conclusion of this study, we used a FITS image
208 provided by the ALMA observatory.

209 **D Flux measurements**

To investigate the spectral index at the centimetre/millimetre in selected apertures (circles in Extended Data Figures 1 and 2), we measured the flux densities using the `imstat` command in Common Astronomy Software Applications package (CASA)⁴⁴. To measure the fluxes in high-resolution images, we smoothed the images into a 0.15 arcsec beam using the `imsmooth` task in CASA to reduce systematic errors due to beam dilution. Table 2 summarises the flux density (S_ν) measurements. The error of the measured flux density is estimated in two ways. First, we used the noise level of the image data,

$$\sigma_1 = \text{rms} \sqrt{\frac{N_S}{N_B}}, \quad (3)$$

where N_S is the number of pixels inside the aperture and N_B is the number of pixels inside the synthesized beam. The root mean square (rms) values are listed in Table 1. This error was used to evaluate the signal-to-noise (S/N) ratio. For example, the 14.9 GHz emission around P1 was detected with $S/N = 12 (= 1.54/0.128)$. In addition, this error was used when we compared the flux density at each region for the same data. For example, in the case of 92.0 GHz high-resolution data, the flux density associated with P2 ($S_\nu = 0.972 \pm 0.030$ mJy) was higher than that of P4 ($S_\nu = 0.795 \pm 0.030$ mJy). However, when we compared our measurements with the multi-wavelength data obtained using different telescopes, a large systematic error due to the calibration process was observed. We applied a 10% systematic error for both the VLA and ALMA data,

$$\sigma_2 = \sqrt{\sigma_1^2 + (0.1S_\nu)^2}. \quad (4)$$

210 For example, the absolute flux calibration error for ALMA bands 3 and 6 is $< 5\%$, according to the ALMA technical
 211 handbook. However, uncertainties due to imaging (e.g. clean parameters) and calibration processes may lead to
 212 systematic errors. Therefore, we used 10% as a conservative estimation. We applied the flux measured at P2 within
 213 the aperture of 0.15 arcsec diameter and obtained $S_\nu = 0.77$ mJy, which is not consistent with the results obtained for
 214 0.2 arcsec diameter as shown in Table 2.

215 **E Spectral index measurements**

216 We investigated the spectral index α based on the VLA and ALMA flux measurements (Figure 3). The index is
 217 calculated using least squares fitting, and the fitting error is based on the scatter and number of measured values.
 218 For the global properties (i.e. NE-Lobe), the spectral index was calculated as $\alpha = 0.77 \pm 0.04$. Here, the 223.7 GHz
 219 measurements were not used because the maximum recovered scale was smaller than that of the VLA images (Table 1).
 220 In the head region, a slightly flatter index ($\alpha = 0.70 \pm 0.04$) than that of the global lobe was measured. Using the
 221 high-resolution data, we measured the local spectral indices at P1 ($\alpha = 0.50 \pm 0.16$), P2 ($\alpha = 0.59 \pm 0.14$), P3
 222 ($\alpha = 0.65 \pm 0.10$), P4 ($\alpha = 0.50 \pm 0.09$), T1 ($\alpha = 0.60 \pm 0.02$), and T2 ($\alpha = 0.47 \pm 0.06$). For the high-resolution
 223 data, the maximum recovery scale (MRS) of the 92.0 GHz ALMA band 3 data was lower than that of the 14.9 GHz
 224 VLA and 252.4 GHz ALMA band 6 data. Because the 92.0 GHz flux was not smaller than the fluxes of 14.9 GHz VLA
 225 and ALMA band 6, the missing flux for band 3 data is negligible when we investigate small local areas. Although there
 226 are uncertain issues related to the missing flux that impede the measurement of the spectral index, our measurements
 227 show that $\alpha \approx 0.5$ is preferred to hard ($\alpha > 1$) or flat ($\alpha \approx 0$) indices at the parsec-scale blobs.

228 **F Origin of millimetre continuum emission**

229 In this study, we considered the millimetre radio emission to be synchrotron radiation, based on the derived spectral
 230 index, α . Another millimetre origin, rather than a synchrotron, is shock-compressed Bremsstrahlung-emitting gas
 231 produced from the jet and ISM interactions. Such a structure was confirmed at the ring around the $10 M_\odot$ black
 232 hole in the Cygnus X-1 X-ray binary system⁴³. However, we rejected this parameter to explain the 92 GHz map at
 233 the jet head of NGC 1068. The observed $S_\nu \approx 0.77$ mJy with an emission volume of $V \approx 8.7 \times 10^2 \text{ pc}^3$ can be
 234 explained by considering a high electron density ($n_e > 1000 \text{ cm}^{-3}$). In such dense regions, the free-free cooling

timescale is considerably shorter than the jet timescale, implying that the radiation distance should be very small, which is not consistent with the resolved 92 GHz ALMA map. The Bremsstrahlung emission may originate from in-situ star formation. However, strong recombination lines were not detected at the jet tip^{45,46}. Therefore, the non-thermal synchrotron radiation is more reasonable than the thermal Bremsstrahlung to explain the resolved 92 GHz ALMA map. Instead, the X-ray spectrum was explained by two Bremsstrahlung components with temperatures of 0.39 keV and 2.84 keV⁴⁷, because of the interaction between the jet and diffused medium, where the free-free cooling timescale is considerably longer than the jet timescale.

G One-dimensional brightness profile

We used the 1-D Slice tool in the viewer implemented in CASA to create Figure 2. The direction of the line is from the central black hole (RA, DEC) = (02h42m40.71s, -00d00m47.945s) to P2. The profile was fitted with three Gaussian functions using the `curve_fit` task in the Python SciPy module. The error of the best-fit value was estimated as the 95 % confidence interval; for example, $A = 0.175 \pm 0.006$ mJy, $x_{\text{off}} = 0.967 \pm 0.003$ arcsec, and $\text{FWHM} = 0.1472 \pm 0.003$ arcsec for the red curve. In this case, the most important parameter is FWHM, which is approximately three times larger than the synthesized beam size of ≈ 0.05 arcsec.

H Equipartition magnetic field strength.

For synchrotron emission, radio luminosity is described as

$$L_\nu = A(\alpha)V\kappa B^{1+\alpha}\nu^{-\alpha} \quad (5)$$

where $A(\alpha) = 2.344 \times 10^{-25} (1.253 \times 10^{37})^\alpha a(p)$, $a(p) = 0.529$ is constant when $p = 2\alpha + 1 = 2$, and the electron energy spectrum per unit volume is $N(E)dE = \kappa E^{-p}dE$ (all values in SI units)⁴⁸. We assumed equipartition between the electron energy (W_e) and magnetic field energy ($W_B = VB^2/(2\mu_0)$), where $\mu_0 = 1.3 \times 10^{-6} \text{ m kg}^{-2} \text{ A}^{-2}$). Here, W_e is expressed as

$$\begin{aligned} W_e &= V \int_{E_{\min}}^{E_{\max}} E \kappa E^{-p} dE \\ &= \frac{1}{2} V \kappa \log \left(\frac{\nu_{\max}}{\nu_{\min}} \right) \quad (\text{when } p = 2) \\ &= \frac{L_\nu}{2A(\alpha)} B^{-\frac{2}{3}} \nu^{\frac{1}{2}} \log \left(\frac{\nu_{\max}}{\nu_{\min}} \right). \end{aligned} \quad (6)$$

$W_e + W_B$ varies with respect to B , and has a minimum value at

$$\begin{aligned} B_{\min} &= \left[\frac{3\mu_0}{4V} \frac{L_\nu}{A(\alpha)} \nu^{-\frac{1}{2}} \log \left(\frac{\nu_{\max}}{\nu_{\min}} \right) \right]^{\frac{2}{7}} \\ &\approx 230 \mu\text{G} \left(\frac{L_{92\text{GHz}}}{2.5 \times 10^{19} \text{ W Hz}^{-1}} \right)^{\frac{2}{7}} \left(\frac{V}{8.7 \times 10^2 \text{ pc}^3} \right)^{-\frac{2}{7}}, \end{aligned} \quad (7)$$

where $\nu_{\min} = 15$ GHz, $\nu_{\max} = 250$ GHz, and $\nu = 92$ GHz. B_{\min} corresponds approximately to the equality of the energies in the relativistic electrons and the magnetic field. The equipartition magnetic field is then defined as $B_{\text{eq}} = B_{\min}$. We note that the equipartition considering electron energy (not total particle energy, including protons) gives the minimum value of the equipartition magnetic field. Therefore, our estimation indicates that the magnetic field is stronger than $B = 230 \mu\text{G}$ under any equipartition requirement. (SI units are used only in this section; in the other sections, cgs units have been used).

256 **I Cosmic-ray maximum energy**

The maximum cosmic-ray energy can be calculated using Eq. 6 in Ref⁴⁹ as

$$E_{\text{cr,max}} = 8 \text{ PeV} \left(\frac{n_e}{1 \text{ cm}^{-3}} \right)^{\frac{1}{2}} \left(\frac{v_{\text{shock}}}{3.0 \times 10^3 \text{ km s}^{-1}} \right)^3 \left(\frac{t_{\text{age}}}{1.3 \times 10^5 \text{ yr}} \right) \left(\frac{p_{\text{cr}}/\rho v_{\text{shock}}^2}{0.3} \right), \quad (8)$$

where n_e is the electron density, t_{age} is the age of the system, and $p_{\text{cr}}/\rho v_{\text{shock}}^2$ is the cosmic-ray pressure ratio at the shock. For NGC 1068, we apply $n_e = 1 \text{ cm}^{-3}$ (as a typical ISM value), $v_{\text{shock}} = 3.0 \times 10^3 \text{ km s}^{-1}$, $t_{\text{age}} = t_{\text{jet}} = 1.3 \times 10^5 \text{ yr}$, and $p_{\text{cr}}/\rho v_{\text{shock}}^2 = 0.3$ (assuming the same situation as in the supernova cases). The maximum cosmic-ray energy can also be predicted on the basis of the requirement that “the cosmic-ray acceleration timescale (t_{accel}) cannot exceed the age of the system”. Using the common assumption of Bohm diffusion, the cosmic-ray acceleration timescale was estimated to be $t_{\text{accel}} \approx (10\eta_B cr_g)/(3v_{\text{shock}}^2)$, where $r_g = E_{\text{cr}}/eB$ is the gyroradius and η_B is the Bohm factor. When we apply t_{adv} (the shortest time among t_{adv} , t_{sync} , and t_{jet}) as the age of the system, the maximum cosmic-ray energy ($E_{\text{cr,max}}$) is given by

$$\begin{aligned} E_{\text{cr,max}} &\approx \frac{3e}{10c} \eta_B^{-1} B v_{\text{shock}}^2 t_{\text{adv}} \\ &\approx 2.5 \eta_B^{-1} \text{ PeV} \left(\frac{B}{230 \mu\text{G}} \right) \left(\frac{v_{\text{shock}}}{3.0 \times 10^3 \text{ km s}^{-1}} \right)^2 \left(\frac{t_{\text{adv}}}{1.6 \times 10^4 \text{ yr}} \right), \end{aligned} \quad (9)$$

257 Both these estimates yield a cosmic-ray maximum energy of $\approx \text{PeV}$.

258

259 **J Possibility of non-equilibrium situation.**

260 Notably, equipartitioning may not be necessary, because if we assume no amplification of the magnetic field (non-
 261 equipartition), then the typical ISM magnetic field ($B \approx 5 \mu\text{G}$) should be applied to explain the 92 GHz flux of the
 262 blob. In this case, a higher U_e than that of the equipartition case is required (e.g. $U_e = 9 \times 10^{-7} \text{ erg cm}^{-3}$ when
 263 $B = 5 \mu\text{G}$), indicating that the total electron power in “one” blob is $P_e = 3 \times 10^{41} \text{ erg s}^{-1}$ and $P_{\text{CR}} = 3 \times 10^{43} \text{ erg s}^{-1}$,
 264 which exceeds $P_{\text{jet}} = 1.8 \times 10^{43} \text{ erg s}^{-1}$. Finally, the magnetic field strength higher than B_{eq} , for example, $B >$
 265 $1000 \mu\text{G}$, is difficult to explain using the known physical models for magnetic field intensity amplification. Therefore,
 266 we applied $B = B_{\text{eq}} = 230 \mu\text{G}$ as a feasible estimate, and the assumption of equipartition provides a physically
 267 reasonable scenario to explain the particle acceleration at the blobs.

268 **K Other notes.**

269 The origin of the parallel arc-like structure remains unresolved. One possible explanation is the separated shock due
 270 to delayed jet activities. For example, the separation between two arcs ($\Delta l \approx 20 \text{ pc}$ which is measured by x_{off} of the
 271 red and green curves in Figure 2) indicates the time delay of multi-episodic jet activities, and $\Delta t = (3/5)(\Delta l/v_{\text{exp}}) \approx$
 272 $4 \times 10^3 \text{ yr}$. Another possible explanation is that the two arcs correspond to the near and far sides of the cone tip,
 273 implying that modelling three-dimensional distribution of accelerated electrons is possible through a resolved map.
 274 However, the current dataset cannot distinguish between these two scenarios.

275

276

278 31. Astropy Collaboration *et al.* The Astropy Project: Building an Open-science Project and Status of the v2.0 Core
279 Package. *AJ* **156**, 123 (2018). 1801.02634.

277

280 32. Astropy Collaboration *et al.* Astropy: A community Python package for astronomy. *Astron. Astrophys.* **558**, A33
281 (2013). 1307.6212.

282 33. Seyfert, C. K. Nuclear Emission in Spiral Nebulae. *Astrophys. J.* **97**, 28 (1943).

283 34. Tully, R. B. & Fisher, J. R. *Catalog of Nearby Galaxies* (1988).

284 35. García-Burillo, S. *et al.* Molecular line emission in NGC 1068 imaged with ALMA. I. An AGN-driven outflow
285 in the dense molecular gas. *Astron. Astrophys.* **567**, A125 (2014). 1405.7706.

286 36. Gallimore, J. F., Baum, S. A. & O’Dea, C. P. The Subarcsecond Radio Structure in NGC 1068. II. Implications
287 for the Central Engine and Unifying Schemes. *Astrophys. J.* **464**, 198 (1996).

288 37. Bland-Hawthorn, J. *et al.* The Ringberg Standards for NGC 1068. *Ap&SS* **248**, 9–19 (1997).

289 38. Wilson, A. S., Elvis, M., Lawrence, A. & Bland-Hawthorn, J. An X-Ray Image of the Seyfert Galaxy NGC 1068.
290 *Astrophys. J. Lett.* **391**, L75 (1992).

291 39. Tecza, M., Thatte, N. & Maiolino, R. Probing the heart of an active galactic nucleus: NGC 1068. In Schilizzi,
292 R. T. (ed.) *Galaxies and their Constituents at the Highest Angular Resolutions*, vol. 205, 216 (2001).

293 40. Cecil, G. *et al.* Spatial Resolution of High-Velocity Filaments in the Narrow-Line Region of NGC 1068: Associ-
294 ated Absorbers Caught in Emission? *Astrophys. J.* **568**, 627–638 (2002). astro-ph/0112256.

295 41. Bîrzan, L., McNamara, B. R., Nulsen, P. E. J., Carilli, C. L. & Wise, M. W. Radiative Efficiency and Con-
296 tent of Extragalactic Radio Sources: Toward a Universal Scaling Relation between Jet Power and Radio Power.
297 *Astrophys. J.* **686**, 859–880 (2008). 0806.1929.

298 42. Kaiser, C. R. & Alexander, P. A self-similar model for extragalactic radio sources. *Mon. Not. R. Astron. Soc.* **286**,
299 215–222 (1997).

300 43. Gallo, E. *et al.* A dark jet dominates the power output of the stellar black hole Cygnus X-1. *Nature* **436**, 819–821
301 (2005). astro-ph/0508228.

302 44. McMullin, J. P., Waters, B., Schiebel, D., Young, W. & Golap, K. CASA Architecture and Applications. In Shaw,
303 R. A., Hill, F. & Bell, D. J. (eds.) *Astronomical Data Analysis Software and Systems XVI*, vol. 376 of *Astronomical*
304 *Society of the Pacific Conference Series*, 127 (2007).

305 45. Venturi, G. *et al.* MAGNUM survey: Compact jets causing large turmoil in galaxies. Enhanced line widths
306 perpendicular to radio jets as tracers of jet-ISM interaction. *Astron. Astrophys.* **648**, A17 (2021). 2011.04677.

307 46. Mingozzi, M. *et al.* The MAGNUM survey: different gas properties in the outflowing and disc components in
308 nearby active galaxies with MUSE. *Astron. Astrophys.* **622**, A146 (2019). 1811.07935.

309 47. Young, A. J., Wilson, A. S. & Shopbell, P. L. A Chandra X-Ray Study of NGC 1068. I. Observations of Extended
310 Emission. *Astrophys. J.* **556**, 6–23 (2001). astro-ph/0104027.

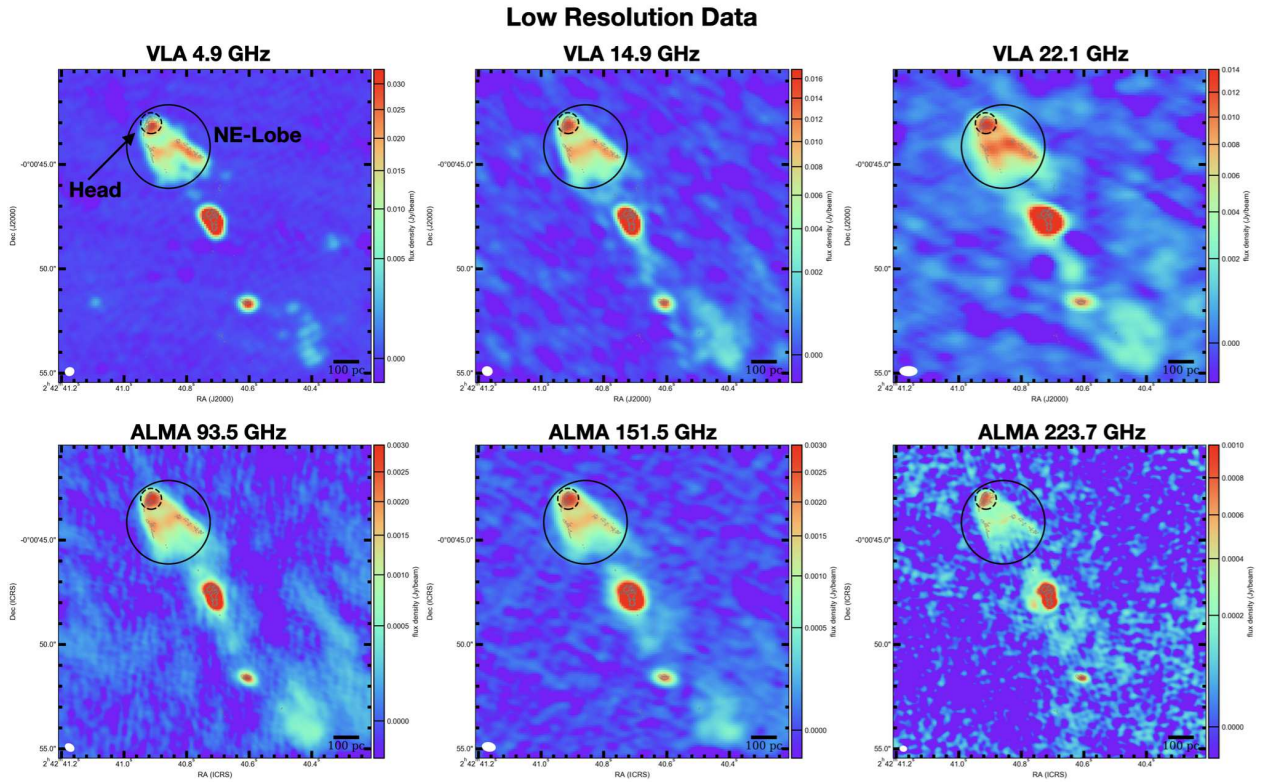
311 48. Longair, M. S. *High Energy Astrophysics* (2011).

312 49. Bell, A. R., Schure, K. M., Reville, B. & Giacinti, G. Cosmic-ray acceleration and escape from supernova
313 remnants. *Mon. Not. R. Astron. Soc.* **431**, 415–429 (2013). 1301.7264.

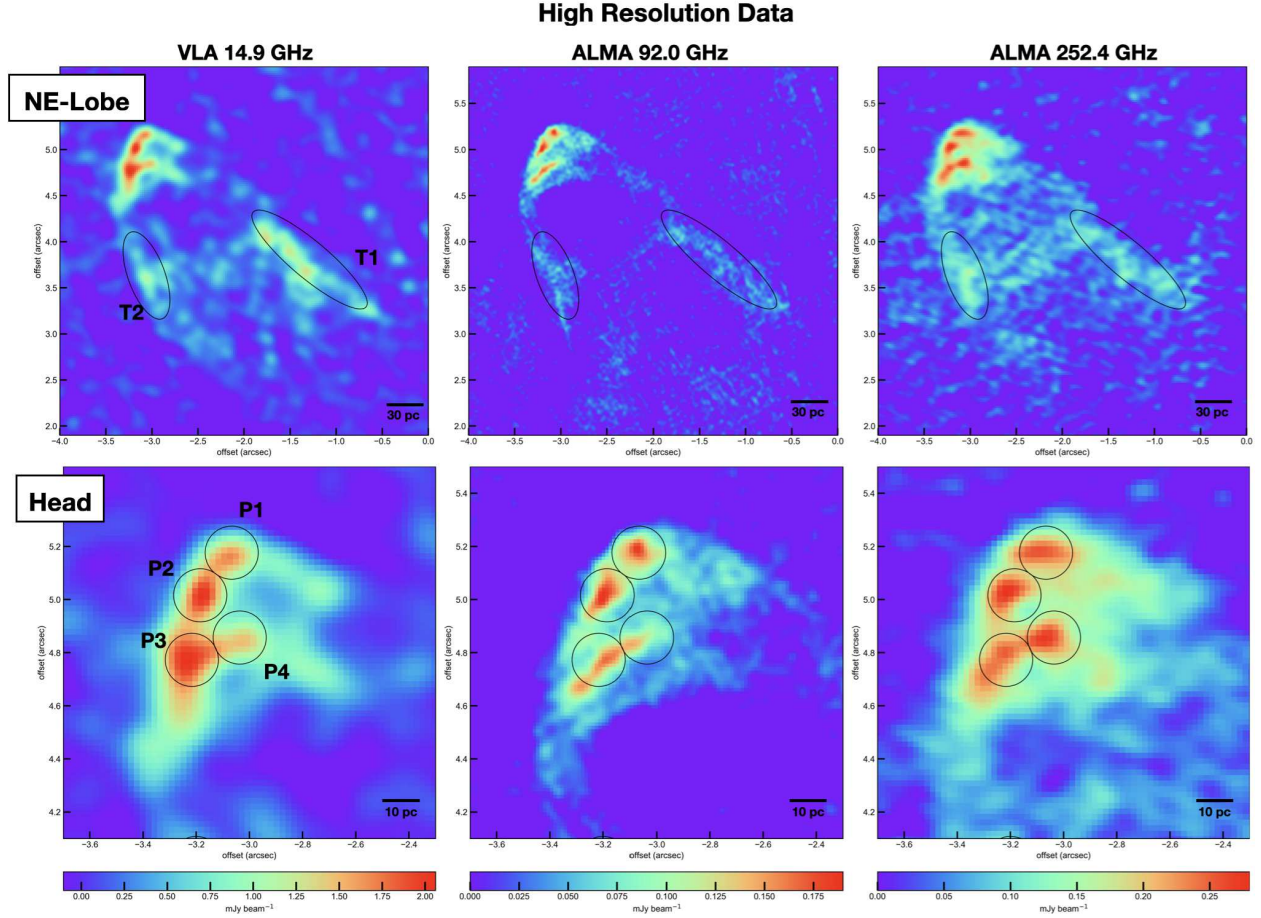
314 **Acknowledgements** Some of the ALMA data were retrieved from the JVO portal (<http://jvo.nao.ac.jp/portal/>)
315 operated by ADC/NAOJ. Data analysis was in part carried out on the common use data analysis computer system at the Astronomy
316 Data Center, ADC, of the National Astronomical Observatory of Japan. This letter makes use of the following ALMA data:
317 #2018.1.01135, #2018.1.01506, #2015.1.01144, #2016.1.00232, #2016.1.00023. ALMA is a partnership of ESO (representing
318 its member states), NSF (USA) and NINS (Japan), together with NRC (Canada), NSC and ASIAA (Taiwan), and KASI (Republic
319 of Korea), in cooperation with the Republic of Chile. The Joint ALMA Observatory is operated by ESO, AUI/NRAO and NAOJ.

320 **Author Information** Reprints and permissions information is available at www.nature.com/reprints. The authors declare no
321 competing financial interests. Readers are welcome to comment on the online version of this study.

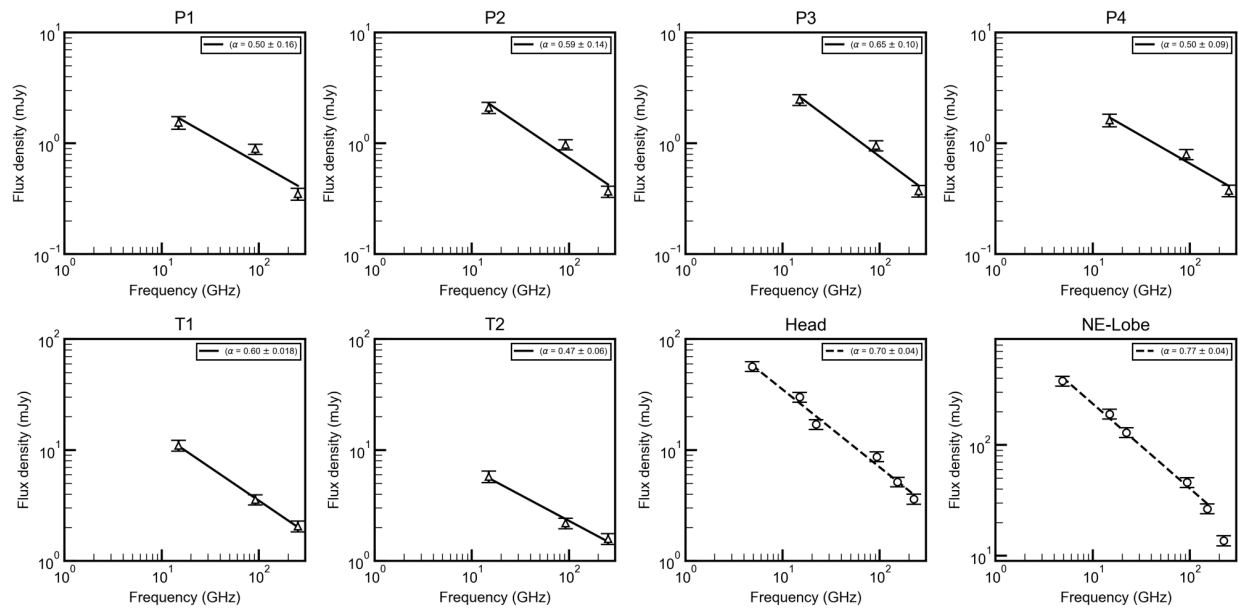
322 **Author Contributions** T.M. led the project. Y.I. and D.K. contributed to the theoretical estimations. A.D. contributed to the
323 analysis of the ALMA and VLA data.



Extended Data Figure 1: Low-resolution VLA and ALMA images. The solid black circles indicate the 4 arcsec aperture around $(RA, DEC) = (02h42m40.858s, -00d00m44.144s)$ used to measure the global properties of the lobe (NE-Lobe). The dashed circles indicate the 1 arcsec aperture around $(RA, DEC) = (02h42m40.913s, -00d00m43.023s)$ used to measure the total flux at the tip of the lobe (head). The white ellipse in the lower left corner is the synthesized beam. The 100-pc scale bar is shown at the bottom right. The grey contour shows the high-resolution 92 GHz continuum emission.



Extended Data Figure 2: High-resolution VLA and ALMA images. The upper panels are the 4 arcsec images around the NE-Lobe. Limb-brightened ridges on the northwestern and eastern sides of the lobe (T1 and T2) were resolved, and the three-dimensional structure of the lobe resembled a cone. The black ellipsicals indicate the apertures used to measure the flux density associated with T1 and T2. The major and minor radii of the aperture for T1 were 1.6 and 0.4 arcsec, respectively, around (RA, DEC) = (02h42m40.795s, -00d00m44.138s) with a position angle of 50°. The major and minor radii of the aperture for T2 were 1.0 and 0.4 arcsec, respectively, around (RA, DEC) = (02h42m40.913s, -00d00m44.311s) with a position angle of 20°. The lower panels show enlarged views around the head of the NE-Lobe. The 0.2 arcsec aperture around the peaks are shown as black circles (P1, P2, P3 and P4). The central coordinate for each peak is (RA, DEC) = (02h42m40.9135s, -00d00m42.7683s) for P1, (RA, DEC) = (02h42m40.9214s, -00d00m42.9287s) for P2, (RA, DEC) = (02h42m40.9235s, -00d00m43.1716s) for P3, and (RA, DEC) = (02h42m40.9115s, -00d00m43.0876s) for P4. The coordinates are determined in the ALMA images, and the flux for the 14.9-GHz VLA image is measured based on the offset from the nucleus.



Extended Data Figure 3: Spectral index measurements. For P1, P2, P3, P4, T1, and T2, high-resolution data were used to measure the spectral index. For the head and NE-Lobe, low-resolution data were used. The flux density values are shown in Table 2.

Extended Data Table 1: Flux density

telescope	Freq. GHz	Resolution arcsec	rms $\mu\text{Jy beam}^{-1}$	date	band	Config.	MRS arcsec	ALMA ID
– Low resolution data –								
VLA	4.9	0.43×0.39	195	1985-01-14	C	A/A	4.5	–
VLA	14.9	0.49×0.44	133	1984-01-13	U	B/B	6	–
VLA	22.1	0.83×0.45	225	2000-02-23	K	C/B	4-33	–
ALMA	93.5	0.46×0.34	43	2019-09-22,23	3	C43-6	5.5	2018.1.01506.S
ALMA	151.5	0.64×0.42	24	2016-07-19	4	C40-5	4.0 ^{*3}	2015.1.01144.S
ALMA	223.7	0.33×0.36	42	2016-10-30	6	C40-6	1.3 ^{*3}	2016.1.00232.S
– high resolution data –								
VLA	14.9	0.145×0.136	105	1983-11-03	U	A/A	1.8	–
ALMA	92.0	0.053×0.050	8	2019-06-22,24	3	C43-9/10	0.9	2018.1.01135.S
ALMA	252.4	0.150×0.103	19	2017-07-23 ^{*1}	6	C43-6 ^{*2}	3.4	2016.1.00023.S

Note: The values of observed (sky) frequency and resolution are based on the header of the downloaded FITS files. The sensitivity was measured in the emission-free region around the NE-Lobe. The MRS for VLA observations was predicted using a table available on the VLA website. The MRS for ALMA observations was based on the observatory reports (QA2 report), except for 2015.1.01144.S and 2016.1.00232.S.

^{*1} Observations were conducted on 2017-07-23, 2017-07-24, 2017-07-27, 2017-12-27, 2018-01-01, 2018-01-19, and 2018-01-21.

^{*2} Observations were conducted in C40-5 and C43-5 as well.

^{*3} The MRS is predicted based on configuration and receiver band using the data in the table shown in ALMA cycle-6 observer’s guide.

Extended Data Table 2: Flux density

region	freq.	S_ν	σ_1	σ_2
	GHz	mJy	mJy	mJy
NE-Lobe	4.9	376.8	1.6	37.7
NE-Lobe	14.9	190.2	1.0	19.0
NE-Lobe	22.2	129.4	1.2	13.0
NE-Lobe	93.5	45.8	0.4	4.6
NE-Lobe	151.5	26.6	0.2	2.7
NE-Lobe	223.7	13.7	0.5	1.4
Head	4.9	56.7	0.4	5.7
Head	14.9	30.1	0.2	3.0
Head	22.2	17.0	0.3	1.7
Head	93.5	8.71	0.09	0.88
Head	151.5	5.16	0.04	0.52
Head	223.7	3.6	0.12	0.38
T1	14.9	10.97	0.5	1.21
T1	92.0	3.56	0.12	0.38
T1	252.4	2.05	0.5	1.21
T2	14.9	5.76	0.12	0.38
T2	92.0	2.18	0.09	0.23
T2	252.4	1.58	0.39	0.7
P1	14.9	1.54	0.128	0.2
P1	92.0	0.888	0.03	0.094
P1	252.4	0.349	0.024	0.042
P2	14.9	2.102	0.128	0.246
P2	92.0	0.972	0.03	0.102
P2	252.4	0.367	0.023	0.044
P3	14.9	2.472	0.128	0.278
P3	92.0	0.95	0.029	0.099
P3	252.4	0.371	0.023	0.044
P4	14.9	1.616	0.128	0.206
P4	92.0	0.795	0.03	0.085
P4	252.4	0.373	0.024	0.044

Note: The apertures of each region are shown in Figures 1 and 2.